International Forum on Aeroelasticity and Structural Dynamics
IFASD 2026
16-19 June 2026, Goettingen, Germany

DESIGN-ORIENTED STRESS-BASED HIGH-FIDELITY AEROELASTIC GUST COMPUTATIONS

Bret K. Stanford[1], **Andrew S. Thelen**[1], **Kevin E. Jacobson**[1]

[1]NASA Langley Research Center, Aeroelasticity Branch
MS 340, Hampton, VA, 23681, USA
bret.k.stanford@nasa.gov
andrew.s.thelen@nasa.gov
kevin.e.jacobson@nasa.gov

Keywords: gust response, CFD, adjoint derivatives

Abstract: Aeroelastic response of a wing structure due to a discrete gust is commonly computed with linear doublet lattice aerodynamics, corrected in some way for transonic flows. The aeroelastic response is computed in the modal space, and the key output of interest is some linear function of those modes, for example root bending moment. This work seeks to expand this analysis to include stress-based outputs (with the modal acceleration method) and aerodynamics based on computational fluid dynamics, as well as adjoint derivatives with respect to shape and structural sizing variables. Examples are shown for generic wingbox structures under both prescribed oscillatory loading and discrete aeroelastic gust loading.

1 INTRODUCTION

The state-of-the-practice in industry for aeroelastic gust computations uses linear doublet lattice method (DLM) aerodynamics [1] in the frequency domain coupled to a modal representation of the structure [2]. Continuous and discrete gust loads may be computed using various techniques [3], with the latest certifications requirements listed in FAR-25 [4]. These linear aeroelastic gust tools, with steady correction factors (to account for transonic effects) computed from wind tunnel or numerical data [5], have been successfully used for transport aircraft design for many years. Future trends in aircraft design, however, will include longer and thinner wings in an effort to reduce environmental impact and operational costs [6]. The aeroelastic tools that have governed past success may not translate to future nontraditional configurations, where the gust mechanisms, and the ensuing wing designs, will be far more complex.

Transonic flows in particular may lead to an overly aggressive aeroelastic gust mechanism. Approaches based on correction factors [7] may be able to properly account for these mechanisms, or a full accounting via computational fluid dynamics (CFD) may be required. CFD-based gust computations in the time domain are very expensive [8, 9, 10], particularly in a design-oriented setting, where reverse-time adjoint computations are required [11]. CFD-based gust computations using the linearized frequency domain (LFD) method have been shown to provide high fidelity gust predictions at a reduced cost [12, 13] and are more amenable to adjoint-based sensitivity computations [14, 15]. The linearization can, however, lead to inaccuracies as well. Ref. [16] has shown that, for higher gust load amplitudes, a linearized computation can over-predict the bending moments relative to a fully-nonlinear time domain computation, but under-predict the torsional moments.

The findings of Ref. [16] highlight another issue with state-of-the-practice aeroelastic gust computations, which is that most of these tools utilize bending and torsional moment results as a structural failure metric. Stress-based metrics and derivatives are more relevant for complex wingbox structures but are relatively difficult to accurately extract from a modal structural approximation [17, 18]. Furthermore, stress-based failure indices (von Mises, VM, for metallic structures, Tsai-Wu for composite structures, etc.) are nonlinear quadratic functions of the modal response, and this can complicate certain gust response formulations [19].

The goals of this work are to advance the state-of-the-practice in computational aeroelastic gust analysis by computing peak stresses (in time) of an aeroelastic wingbox, in response to a discrete gust input, using a modal structural finite element solver and an LFD-based aerodynamic solver implemented in the FUN3D flow solver [20, 21]. Stresses are computed with the well-known modal acceleration (MA) method [17, 22, 23]. Coupling between the various solvers is enabled with OpenMDAO [24] and MPhys [25], which allow for the computation of analytical adjoint derivatives of the peak stress with respect to a large vector of shape and sizing parameters.

Results in this paper will first demonstrate the MA computations and adjoint derivatives on a generic transport configuration driven by a prescribed (non-aerodynamic) unsteady loading. Exact stress computations are available for this case, which allows errors related to the modal approximation to be quantified. Next, aeroelastic gust loadings are computed. A key aspect of the MPhys-based tool is the ease with which one discipline's fidelity can be swapped for another. Given this enabling feature, gust response results will be demonstrated with both linear DLM aerodynamics and transonic LFD-based aerodynamics, an extension of past work from Refs. [14, 15]. Finally, the computation and validation of adjoint derivatives of the stress-based gust response will be demonstrated.

2 AEROELASTIC FRAMEWORK

The modal aeroelastic equations of motion are given in the Laplace domain as:

$$(s^2 \cdot \overline{\boldsymbol{M}} + s \cdot \overline{\boldsymbol{C}} + \overline{\boldsymbol{K}} - q \cdot \overline{\boldsymbol{A}}^{ss}) \cdot \boldsymbol{\eta} = q \cdot \overline{\boldsymbol{A}}^{sg} \cdot w_g/U \tag{1}$$

where $\boldsymbol{M}$, $\boldsymbol{C}$, $\boldsymbol{K}$, and $\boldsymbol{A}$ are the mass, damping, stiffness, and aerodynamic matrices, respectively, and the overbar designates a modally-reduced quantity. The vector $\boldsymbol{\eta}$ is the vector of modal amplitudes, s is the Laplacian, q is the dynamic pressure, U is the flow speed, and w_g is the speed of the vertical gust column. The ss and sg superscripts designate structure-on-structure and gust-on-structure partitioning of the aerodynamic terms.

These results are computed for a discrete gust with a $1 - cos$ profile, where w_g is a Fourier transform of that function. An inverse Fourier transform [2] of $\boldsymbol{\eta}$ will provide these modal amplitudes as a function of time. The modal amplitudes are converted into a stress distribution at each time step (as detailed below), the stress distribution is aggregated into a single scalar metric at each time step [26], and finally the maximum aggregate value (in time) is extracted for design optimization purposes. Alternatively, $\boldsymbol{\eta}$ may be left in the frequency domain to compute the stresses in the frequency domain also; the stresses can then transformed via an inverse Fourier transform, and the process proceeds as in the first option. Either option will give the same answer, but the computational effort will vary.

2.1 Modal Acceleration

If the matrix of structural mode shapes is given by $\boldsymbol{\phi}$, then the full-order structural response vector is $\boldsymbol{u} = \boldsymbol{\phi} \cdot \boldsymbol{\eta}$. Plane stress in a given finite element can be computed as:

$$\left\{ \begin{array}{c} \sigma_x \\ \sigma_y \\ \sigma_{xy} \end{array} \right\}_e = \boldsymbol{B}_{\sigma_e} \cdot \boldsymbol{u} \tag{2}$$

where the matrix $\boldsymbol{B}_{\sigma_e}$ is different for each element e.

As noted previously, computing these stresses as $\boldsymbol{B}_{\sigma_e} \cdot \boldsymbol{\phi} \cdot \boldsymbol{\eta}$ (a formulation commonly called the modal displacement method, MD) is inaccurate, as stress is not easily extracted from a modal reduction. The more accurate MA method is computed as [17]:

$$\boldsymbol{u}_{MA} = \boldsymbol{\phi} \cdot \boldsymbol{\eta} + \boldsymbol{K}^{-1} \cdot \boldsymbol{F} - \boldsymbol{\phi} \cdot \overline{\boldsymbol{K}}^{-1} \cdot \boldsymbol{\phi}^T \cdot \boldsymbol{F} \tag{3}$$

The first term in Eq. 3 is simply the MD approach, and the second two terms are additional enrichment that improves the accuracy of the stress results when computed as $\boldsymbol{B}_{\sigma_e} \cdot \boldsymbol{u}_{MA}$. These enrichment terms are driven by a full-order force vector, $\boldsymbol{F}$, defined as:

$$\boldsymbol{F} = q \cdot \boldsymbol{A}^{ss} \cdot \boldsymbol{\eta} + q \cdot \boldsymbol{A}^{sg} \cdot w_g / U \tag{4}$$

The terms $\boldsymbol{A}^{ss}$ and $\boldsymbol{A}^{sg}$ are partial full-order aerodynamic terms: the rows of these matrices remain in the modal space, but the columns are in the full-order finite-element space [22]. These matrices are related to the overlined modal terms in Eq. 1 as $\overline{\boldsymbol{A}}^{ss} = \boldsymbol{\phi}^T \cdot \boldsymbol{A}^{ss}$ and $\overline{\boldsymbol{A}}^{sg} = \boldsymbol{\phi}^T \cdot \boldsymbol{A}^{sg}$.

As noted above, frequency-domain versions of $\boldsymbol{F}$, $\boldsymbol{\eta}$, and $\boldsymbol{u}_{MA}$ may be utilized in Eqs. 3 and 4. In that case, the stresses can also be computed in the frequency domain, and finally the stresses can be converted into the time domain via an inverse Fourier transform of σ_x, σ_y, and σ_{xy}. Alternatively, inverse Fourier transforms of $\boldsymbol{F}$ and $\boldsymbol{\eta}$ can be used in Eqs. 3 and 4, meaning $\boldsymbol{u}_{MA}$ and the stresses will be directly computed in the time domain. The computational effort of either option is driven by the second term in Eq. 3 ($\boldsymbol{K}^{-1} \cdot \boldsymbol{F}$), which is a linear system of equations with multiple right hand sides, i.e., multiple columns of $\boldsymbol{F}$ in Eq. 4. In the frequency domain, the number of (complex-valued) right hand sides is the number of frequencies considered in Eq. 1. In the time domain, the number of (real-valued) right hand sides is the number of time steps considered in the inverse Fourier transform. The most computationally-efficient choice will be problem-dependent.

2.2 Unsteady Aerodynamics

The CFD-based aerodynamics are computed via the stabilized finite element (SFE [27]) solver in FUN3D [20]. The general flow equations are written as:

$$\boldsymbol{A}(\boldsymbol{q}, \dot{\boldsymbol{q}}, \boldsymbol{x}_G, \dot{\boldsymbol{x}}_G) := \boldsymbol{M}_A(\boldsymbol{q}, \boldsymbol{x}_G, \dot{\boldsymbol{x}}_G) \cdot \dot{\boldsymbol{q}} + \boldsymbol{R}_A(\boldsymbol{q}, \boldsymbol{x}_G, \dot{\boldsymbol{x}}_G) \tag{5}$$

where $\boldsymbol{q}$ is the flow state vector, $\boldsymbol{x}_G$ is the vector of volume mesh coordinates, $\boldsymbol{R}_A$ is the spatial residual, and $\boldsymbol{M}_A$ is the mass matrix. The steady computations over a wing are obtained by setting the time derivatives to zero:

$$\boldsymbol{A}_0(\boldsymbol{q}_0, \boldsymbol{x}_{G_0}) := \boldsymbol{R}_A(\boldsymbol{q}_0, \boldsymbol{x}_{G_0}) = \boldsymbol{0} \tag{6}$$

where the 0 subscript indicates a steady state solution.

One can then assume small oscillatory perturbations of the form $\boldsymbol{x}_G = \boldsymbol{x}_{G_0} + \sum_{j=1}^{n} \hat{\boldsymbol{x}}_{G_j} \cdot e^{i\cdot\omega\cdot t}$, and $\boldsymbol{q} = \boldsymbol{q}_0 + \sum_{j=1}^{n} \hat{\boldsymbol{q}}_j \cdot e^{i\cdot\omega\cdot t}$, where $\hat{\boldsymbol{q}}$ and $\hat{\boldsymbol{x}}_G$ are Fourier coefficients, and ω is the oscillation frequency. Each Fourier coefficient corresponds to a structural mode shape j of interest. Using these assumptions, the LFD equations can be written as:

$$\begin{aligned}&\boldsymbol{A}_{LFD,j}\left(\boldsymbol{x}_{G_0}, \boldsymbol{q}_0, \hat{\boldsymbol{x}}_{G_j}, \hat{\boldsymbol{q}}_j, \omega\right) := \\ &\left(i\cdot\omega\cdot \boldsymbol{M}_A|_{\boldsymbol{x}_{G_0},\boldsymbol{q}_0} + \left.\frac{\partial \boldsymbol{R}_A}{\partial \boldsymbol{q}}\right|_{\boldsymbol{x}_{G_0},\boldsymbol{q}_0}\right)\cdot\hat{\boldsymbol{q}}_j + \left(i\cdot\omega\cdot\left.\frac{\partial \boldsymbol{R}_A}{\partial \dot{\boldsymbol{x}}_G}\right|_{\boldsymbol{x}_{G_0},\boldsymbol{q}_0} + \left.\frac{\partial \boldsymbol{R}_A}{\partial \boldsymbol{x}_G}\right|_{\boldsymbol{x}_{G_0},\boldsymbol{q}_0}\right)\cdot\hat{\boldsymbol{x}}_{G_j} = \boldsymbol{0}\end{aligned} \tag{7}$$

Equation 7 represents a linear complex-valued system of equations, which must be solved once for each structural mode shape j and each frequency value ω of interest.

The complex-valued oscillatory flow fields $\hat{\boldsymbol{q}}_j$ can be used to compute oscillatory aerodynamic forces, $\boldsymbol{f}_{A_j}$ [11]. These aerodynamic forces are mapped onto the structural mesh with the MELD framework [28] (Matching-based Extrapolation for Loads and Displacements) to form $\boldsymbol{f}_{S_j}$. Finally, the $\boldsymbol{A}^{ss}$ term used in Eq. 4 is defined as:

$$\boldsymbol{A}^{ss} = \begin{bmatrix} \boldsymbol{f}_{S_1} & \boldsymbol{f}_{S_2} & \cdots & \boldsymbol{f}_{S_n} \end{bmatrix} \tag{8}$$

A computation of the gust terms proceeds in a similar manner but with an alternate version of Eq. 7:

$$\boldsymbol{A}_{gust,j}\left(\boldsymbol{x}_{G_0}, \boldsymbol{q}_0, \hat{\boldsymbol{x}}_{G_j}, \hat{\boldsymbol{q}}_j, \omega\right) := \left(i\cdot\omega\cdot \boldsymbol{M}_A|_{\boldsymbol{x}_{G_0},\boldsymbol{q}_0} + \left.\frac{\partial \boldsymbol{R}_A}{\partial \boldsymbol{q}}\right|_{\boldsymbol{x}_{G_0},\boldsymbol{q}_0}\right)\cdot\hat{\boldsymbol{q}}_j + \left.\frac{\partial \boldsymbol{R}_A}{\partial \boldsymbol{w}_g}\right|_{\boldsymbol{x}_{G_0},\boldsymbol{q}_0}\cdot\hat{\boldsymbol{w}}_{g_j} = \boldsymbol{0} \tag{9}$$

where $\hat{\boldsymbol{w}}_{g_j}$ is the harmonic gust perturbation field [14]. As above, aerodynamic forces can be mapped and grouped to form $\boldsymbol{A}^{sg}$.

For lower fidelity aerodynamics via the linear DLM, unsteady aerodynamic pressures, for each mode shape and frequency of interest, are computed via the typical complex-valued aerodynamic kernel operations [1]. As with the CFD tools, those unsteady pressures are mapped onto the structural mesh with MELD and then grouped to obtain $\boldsymbol{A}^{ss}$ and $\boldsymbol{A}^{sg}$.

2.3 Analytical Adjoint Derivatives

With the assistance of MPhys [25], separate OpenMDAO components are created for each of the modules used here: steady aerodynamics, unsteady aerodynamics, MELD-based load mapping, structural and modal computations, MA-based stress computations, and finally the inverse Fourier transform. OpenMDAO can automatically handle the forward connections for each component. Each component is individually-tasked with computing analytical adjoint derivatives across its local inputs and outputs; OpenMDAO can then handle the reverse adjoint connections between components for the final derivative of the output (the peak stress aggregate value, in time, during the gust encounter) with respect to a large vector of shape and sizing parameters.

A final stress-based metric is given as $J = J(\boldsymbol{u}_{MA})$, where J will be defined via σ_x, σ_y, and σ_{xy} from Eq. 2. If the various design variables are collected in the vector $\boldsymbol{x}$, the sought-after derivative is computed as:

$$\frac{dJ}{d\boldsymbol{x}} = \frac{\partial J}{\partial \boldsymbol{x}} + \boldsymbol{\lambda}_\eta^T \cdot \frac{\partial \boldsymbol{R}_\eta}{\partial \boldsymbol{x}} + \boldsymbol{\lambda}_\phi^T \cdot \frac{\partial \boldsymbol{R}_\phi}{\partial \boldsymbol{x}} + \boldsymbol{\lambda}_F^T \cdot \frac{\partial \boldsymbol{R}_F}{\partial \boldsymbol{x}} \tag{10}$$

where the residual $\boldsymbol{R}_\eta$ is defined by the solution of Eq. 1, the residual $\boldsymbol{R}_\phi$ is defined by the solution of the structural eigenequations, the residual $\boldsymbol{R}_F$ is defined by the solution of Eq. 4, and the $\boldsymbol{\lambda}$ terms are the associated adjoint vectors. The adjoint vectors are computed as:

$$\left(\frac{\partial \boldsymbol{R}_\eta}{\partial \boldsymbol{\eta}}\right)^T \cdot \boldsymbol{\lambda}_\eta = -\frac{\partial J}{\partial \boldsymbol{\eta}} \tag{11}$$

$$\left(\frac{\partial \boldsymbol{R}_\phi}{\partial \boldsymbol{\phi}}\right)^T \cdot \boldsymbol{\lambda}_\phi = -\frac{\partial J}{\partial \boldsymbol{\phi}} \tag{12}$$

$$\left(\frac{\partial \boldsymbol{R}_F}{\partial \boldsymbol{F}}\right)^T \cdot \boldsymbol{\lambda}_F = -\frac{\partial J}{\partial \boldsymbol{F}} \tag{13}$$

Derivatives of $\boldsymbol{R}_\eta$ are simply computed by differentiating Eq. 1, derivatives of $\boldsymbol{R}_\phi$ are computed via Nelson's method [29], and derivatives of $\boldsymbol{R}_F$ are derived in Ref. [14].

The three right-hand-sides needed in the three adjoint equations are computed by differentiating the modal acceleration equation Eq. 3:

$$\frac{\partial J}{\partial \boldsymbol{\eta}} = \boldsymbol{\phi}^T \cdot \frac{\partial J}{\partial \boldsymbol{u}_{MA}} \tag{14}$$

$$\frac{\partial J}{\partial \boldsymbol{\phi}} = \frac{\partial J}{\partial \boldsymbol{u}_{MA}} \cdot \left(\boldsymbol{\eta} - 2 \cdot \overline{\boldsymbol{K}}^{-1} \cdot \boldsymbol{\phi}^T \cdot \boldsymbol{F}\right) \tag{15}$$

$$\frac{\partial J}{\partial \boldsymbol{F}} = \frac{\partial J}{\partial \boldsymbol{u}_{MA}} \cdot \boldsymbol{K}^{-1} - \frac{\partial J}{\partial \boldsymbol{u}_{MA}} \cdot \left(\boldsymbol{\phi} \cdot \overline{\boldsymbol{K}}^{-1} \cdot \boldsymbol{\phi}^T\right) \tag{16}$$

The explicit derivative of J with respect to the design variables $\boldsymbol{x}$ needed in Eq. 10 is computed via the stiffness matrix (and the reduced stiffness matrix):

$$\frac{\partial J}{\partial \boldsymbol{x}} = -\frac{\partial J}{\partial \boldsymbol{u}_{MA}} \cdot \boldsymbol{K}^{-1} \cdot \frac{\partial \boldsymbol{K}}{\partial \boldsymbol{x}} \cdot \boldsymbol{u}_{MA} + \frac{\partial J}{\partial \boldsymbol{u}_{MA}} \cdot \left(\boldsymbol{\phi} \cdot \overline{\boldsymbol{K}}^{-1} \cdot \boldsymbol{\phi}^T \cdot \frac{\partial \boldsymbol{K}}{\partial \boldsymbol{x}} \cdot \boldsymbol{\phi}\right) \cdot \overline{\boldsymbol{K}}^{-1} \cdot \boldsymbol{\phi}^T \cdot \boldsymbol{F} \tag{17}$$

3 RESULTS

3.1 Non-Aerodynamic Loading

The results shown in this section are for the wingbox (Fig. 1) of the Simple Transonic Wing introduced in Ref. [30]. It is a semispan (14 m) composite wingbox structure consisting of a leading edge spar, a trailing edge spar, upper skins, lower skins, and 23 ribs. The finest L0 mesh from Ref. [30] is used here, with 73,000 shell finite element nodes. A non-aerodynamic oscillatory tip load of 30,000 N is applied to the structure at a frequency of 2 Hz. For reference, the first bending frequency of the structure is 4.2 Hz. Because these are non-aerodynamic loads, and because the input is purely harmonic, the exact stress distribution of the full-order finite element model (without any modal approximation) can be found and benchmarked against MD and MA approximations.

The oscillatory stress distribution (exactly in-phase with the input load, since no structural damping is included here) is shown in Fig. 2, in terms of the Tsai-Wu failure indices of the 90° skin and spar composite fiber plies oriented parallel to the wingbox ribs. These failure

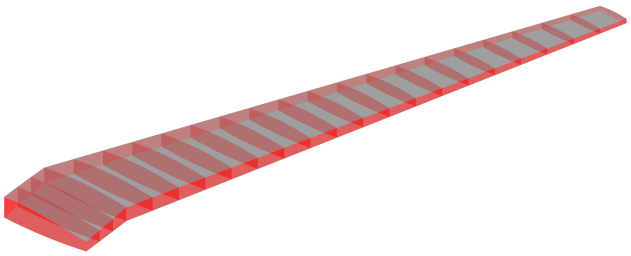


Figure 1: The Simple Transonic Wing's wingbox structure.

indices are nonlinear functions of σ_x, σ_y, and σ_{xy} in each shell finite element. MD and MA results are shown in Fig. 2, both using 3 structural modes, for comparison with the exact results. As expected, the MD results show clear differences from the exact result, whereas the MA result is not visually distinguishable. The stresses in Fig. 2 are then aggregated into a single Kreisselmeier-Steinhauser (KS) scalar, and the log of the error-norms in this scalar are shown in Fig. 3 as a function of the number of modes used in the MD and MA approximations; the latter is consistently 3-4 orders of magnitude better than the former.

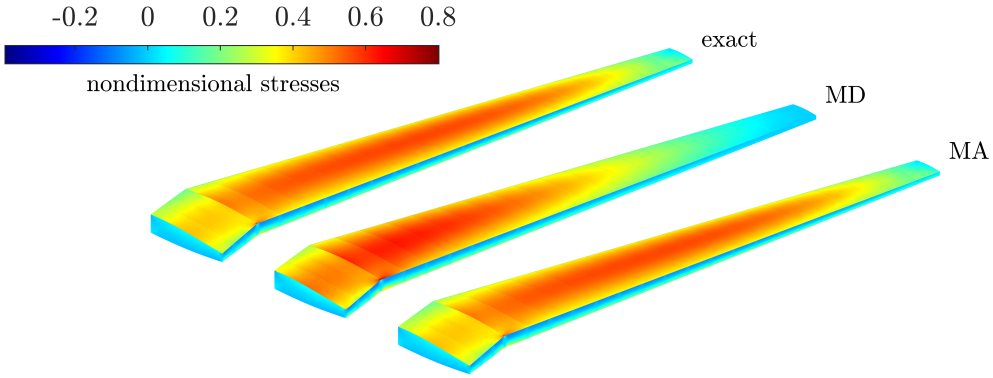


Figure 2: Oscillatory stress distribution in the wingbox.

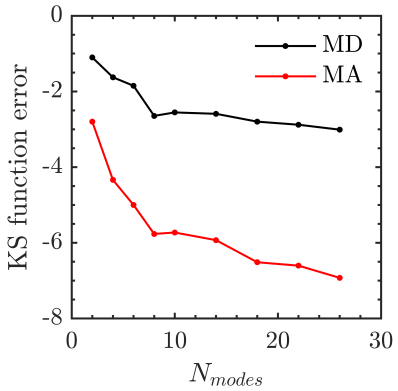


Figure 3: Log scale error norm of the aggregated KS function for both MD- and MA-based approximations.

Next, the derivatives of the KS scalar with respect to the grid coordinates of every finite element node are computed, and the z-coordinate derivative is shown in Fig. 4, again using 3 modes. The strong influence of the rib-skin topology is clearly seen in these shape derivative contour plots, and again, the MD-based method shows strong inaccuracies relative to MA. The quantitative

error norm is shown in Fig. 5, with MA again 3-4 orders of magnitude more accurate.

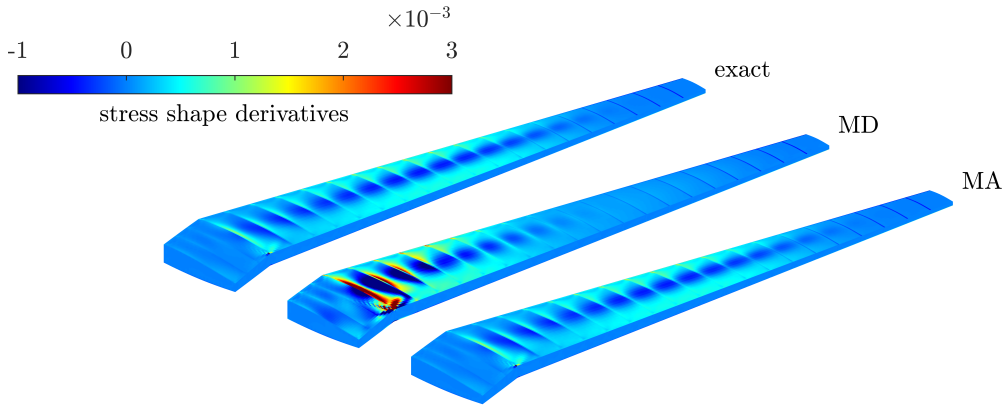


Figure 4: Z-coordinate shape derivatives of the aggregated KS stress metric.

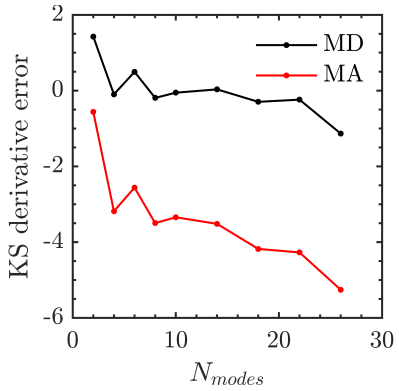


Figure 5: Log scale error norm of the KS function shape derivative for both MD- and MA-based approximations.

3.2 Aeroelastic Gust Loading

The results in this section utilize a wingbox more suitable (compared to the Simple Transonic Wing) for dynamic aeroelastic loading, the Common Research Model (CRM) developed in Ref. [31]. This model is shown in Fig. 6, with a similar wingbox topology as the Simple Transonic Wing, and a lumped mass representation for the leading/trailing edge devices and the nacelle/pylon. These lumped masses ensure that the structural torsional frequency is sufficiently low to induce aeroelastic interactions. This is a metallic model, and so the von Mises stress criteria are used as failure indices, rather than the Tsai-Wu metrics used for the composite wingbox in the previous section. The finite-element mesh is also coarser than used previously, with 9,700 nodes.

The outer mold line of the wing jig shape (also shown in Fig. 6) has a wing span of 58.7 m, a mean aerodynamic chord of 7.0 m, a taper ratio of 0.25, and a quarter-chord sweep angle of 35°. Despite the carry-through topology modeled in the structural finite-element model, the fuselage is not modeled aerodynamically, and the outer mold line simply extends to the symmetry plane of the model. Discrete $1 - cos$ gust loads (superimposed upon a static aeroelastic load) are applied to the wing at Mach 0.85, a flow speed of 254 m/s, and a dynamic pressure of 12.9 kPa. A range of $1 - cos$ gust lengths are utilized between 25 m and 250 m, each with a gust amplitude of 20 m/s.

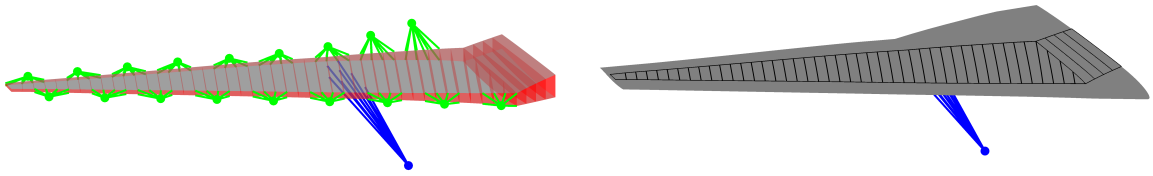


Figure 6: The Common Research Model wingbox structure and lumped mass representation (left) and outer mold line (right).

For the result in Fig. 7, the low-fidelity DLM is used for steady and unsteady aerodynamics, and 9 vibration modes (ϕ) are used for the structural solver. The first two modes are rigid body plunge/pitch modes, but the finite-element model is attached to the ground with very soft springs to prevent the stiffness matrix ($\boldsymbol{K}$) from becoming singular, as required by the modal acceleration computations (Eq. 3) [22]. Figure 7 shows a time history of the von Mises stress in the wingbox, where the peak value of the stress throughout the finite-element model is shown at any given time. As such, minor C-1 discontinuities are seen in Fig. 7, as the location of the peak stress may change from one time step to the next. These stresses are also normalized by the yield stress, such that a value greater than 1 would indicate a structural failure.

Both MD and MA results are shown in Fig. 7 for a gust length of 25 m and 250 m: unlike in the previous section, no exact result is available for these aeroelastic gust simulations. All of the time traces start at a normalized stress of 0.35, which is due to the static aeroelastic loads at an angle of attack (AoA) of 1° (non-trimmed). The longer gust length (250 m) induces higher loads at a lower frequency response and shows sizable differences between MD and MA also. The shorter gust length (25 m) shows no appreciable differences between MD and MA. A sweep of peak gust stress values is shown in Fig. 8, as a function of gust length, and it can be seen that that a gap between MA and MD predictions exist for gust lengths above 100 m.

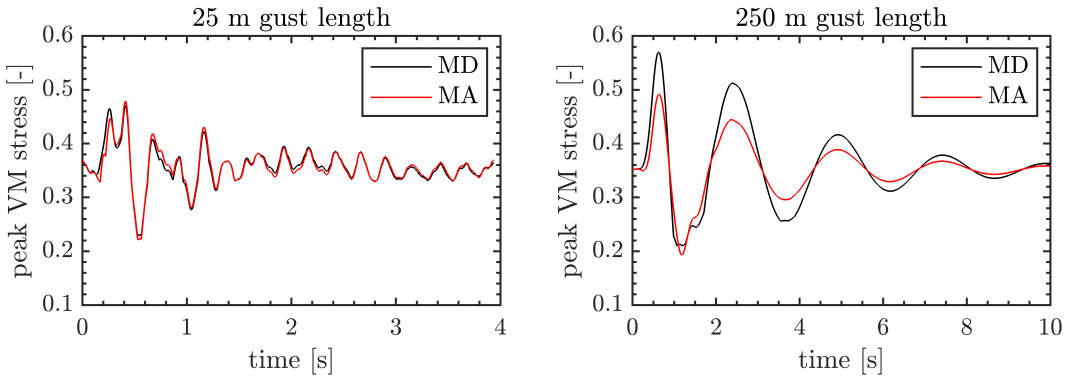


Figure 7: Time history of the peak von Mises stress during the gust encounter.

The static aeroelastic and peak gust stress contours at 250 m are shown in Fig. 9. The gust stresses are shown at a time instance of 0.6 s (corresponding to the first peak in Fig. 7). Stresses are generally largest at the geometry break between the carry-through and the swept wing and also in the wing spar near the geometry break in the outer mold line trailing edge. These latter spar stresses are not well-computed by MD, relative to MA, and is the source of the discrepancy at a 250 m gust length in Fig. 7 also.

As noted above, no exact result is available for these cases, and while there is an expectation

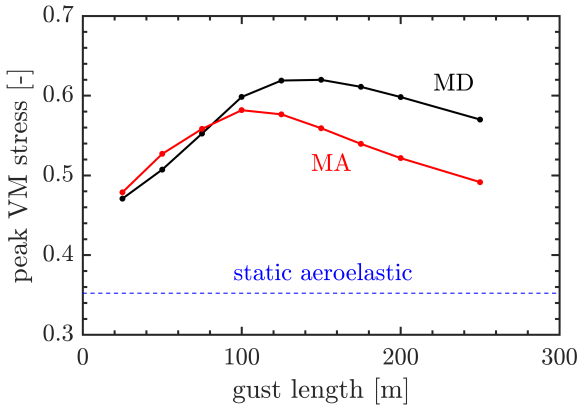


Figure 8: Peak von Mises gust stresses across different gust lengths.

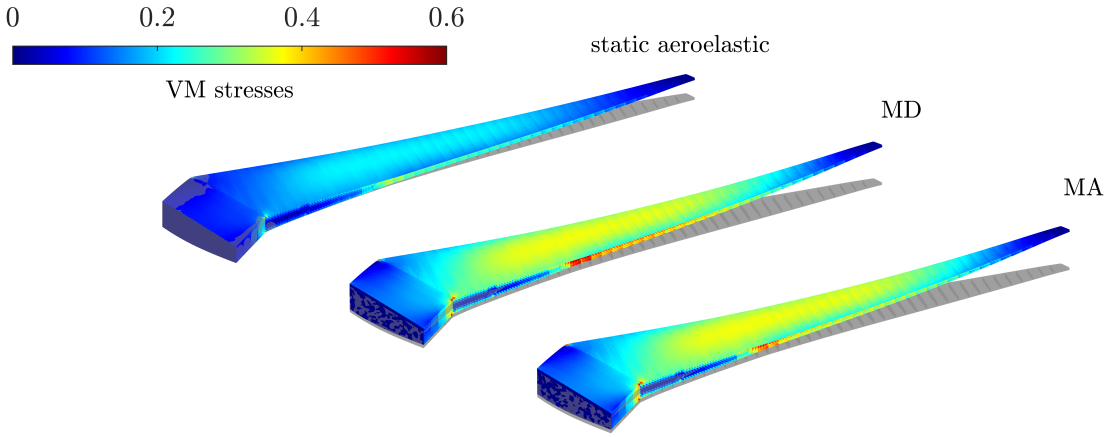


Figure 9: Static aeroelastic stress contours and peak gust stress contours during a gust length of 250 m.

that MD and MA will converge to the same result as the number of included modes increases (with MA converging at a faster rate, as seen in the previous section), this result is challenging to demonstrate in practice due to the unsteady aerodynamics. Both the DLM and the CFD-based LFD tool operate on an array of reduced frequencies (i.e., the oscillation frequency in Eq. 7), and including more modes will require more reduced frequencies, which in turn changes the requirements on the aerodynamic mesh, etc. Table 1 does show, however, that up to the number of modes included in the previous results (nine), the MA-based predictions are much less sensitive to the mode number, compared to MD-based predictions.

Table 1: Modal convergence of the MD- and MA-based peak stresses, for a gust length of 250 m.

number of modes	MD stress	MA stress
3	0.4877	0.4866
5	0.5505	0.4911
7	0.5821	0.4918
9	0.5701	0.4916

The previous results in this section all utilized low-fidelity DLM aerodynamics, and high-fidelity CFD-based results are included next. A range of static aeroelastic CFD results are shown in Fig. 10, using a relatively coarse inviscid mesh with 60,000 nodes. The nacelle/pylon aerodynamics are not modeled here, and so these components only exist inertially (as seen in

Fig. 6). Again using a Mach number of 0.85 and a dynamic pressure of 12.9 kPa, increasing the AoA increases both the static aeroelastic deflection and the strength of the transonic shock.

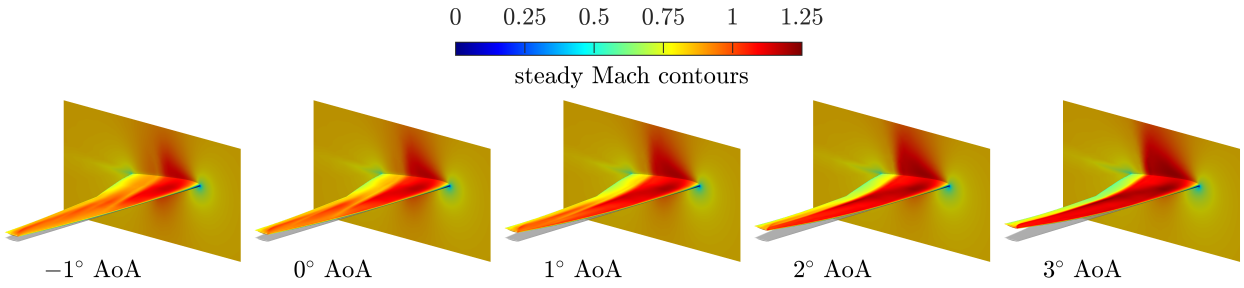


Figure 10: Static aeroelastic Mach contours over the wing.

The dependency of the peak stress upon AoA is shown in Fig. 11. Note, the linear DLM results at 1° are repeated from the previous figures. The figure shows both the peak stress (along the wing) during the static aeroelastic result, and the peak stress (along the wing, and in time) during the gust encounter, all computed with the MA method. For DLM aerodynamics, the static aeroelastic result is obviously a function of AoA, but the unsteady incremental gust loads are not, as linear aeroelasticity is completely separable into static and dynamic terms. As such, the static aeroelastic and gust stress trends computed by DLM are largely parallel versus AoA. The fact that they are not exactly parallel is because of the nonlinear (quadratic) dependency of the von Mises stress upon the state. If some linear metric had been plotted (root bending moment, e.g.) the static and dynamic DLM curves would be exactly parallel. Furthermore, there are some discontinuities in the DLM stress plots between -1 and 0°; this is because the location and mechanism of the peak stress shifts from the wing skins (-1°) to the spar (0°).

For the CFD results, both the static aeroelastic and the gust stresses depend strongly upon AoA, and this effect is more prominent at a gust length of 250 m, compared to 25 m. With increased AoA at 250 m in Fig. 11, the CFD-computed gust increment (i.e., the gap between the static aeroelastic and peak gust stress) increases substantially, as would be expected from the heightened aerodynamic sensitivity in transonic conditions.

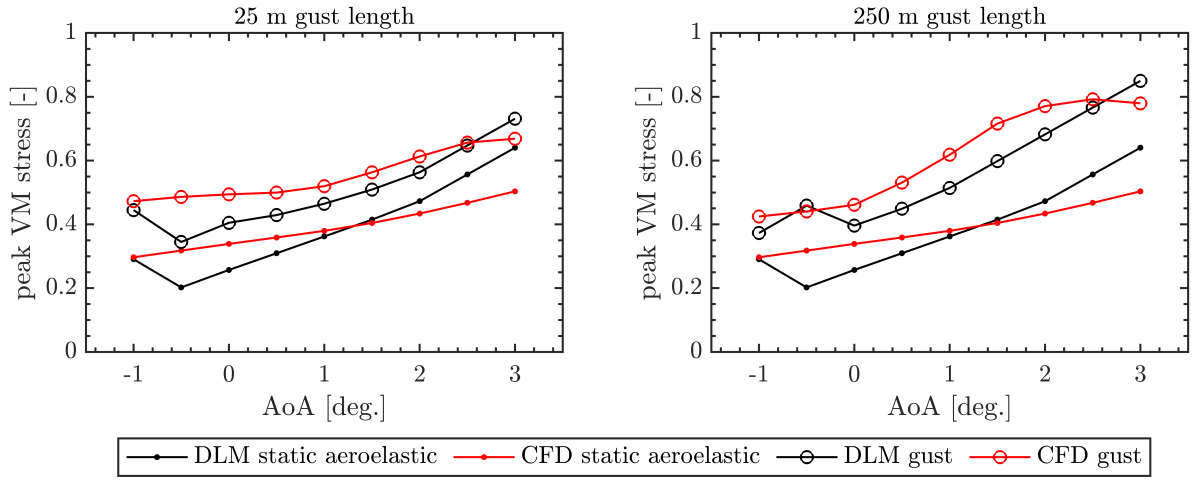


Figure 11: Peak static aeroelastic and gust stresses, as computed with different aerodynamic fidelities.

3.3 Aeroelastic Gust Derivatives

Derivatives of the peak stress seen during the gust response, as computed with Eq. 10, are shown in Table 2. These derivatives are computed with DLM, while higher fidelity CFD-based derivative computations are left for future work. Derivatives with respect to four design variables are shown in the table: two shape variables which morph the planform of the wing (span and sweep), a variable which uniformly scales the thickness of every shell member in the wingbox skins, and a variable which uniformly rotates the orientation of every stiffener in the wingbox skins.

Table 2: Finite difference verifications for adjoint derivative computations.

	span	sweep	shell thickness	stiffener rotation
$\delta = 10^{-1}$	**0.0207**7307	-**0.01103**294	-0.39739819	-0.07549076
$\delta = 10^{-2}$	**0.0207**7811	-**0.0110**2925	-**0.4**2903259	-**0.084**13435
$\delta = 10^{-3}$	**0.0207**4661	-**0.01**097282	-**0.432**48136	-**0.0849**2742
$\delta = 10^{-4}$	**0.020**80855	-**0.011**00512	-**0.43**349744	-**0.08**524694
$\delta = 10^{-5}$	**0.02**247007	-**0.01**070739	-**0.43**349744	-**0.08**524694
analytical	0.02078934	-0.01103300	-0.43288614	-0.08499070

A finite difference step size study is included in the table; more-accurate complex-step perturbations are not possible here, as the forward analysis itself utilizes complex numbers. The four derivatives are generally shown to be accurate, under different step sizes, to within 3-4 decimal places. The rigid body modes used here (seen at the wing root of Figure 9) generally degrade the range of acceptable finite difference step sizes for gust response. Though not shown here, models with a clamped boundary condition have a wider range of acceptable step sizes.

4 CONCLUSIONS

This work has demonstrated the unsteady stress-based response of a wingbox structure to both prescribed loads and aeroelastic gust loads, as well as the derivative of those stresses with respect to a large vector of shape and structural sizing variables. These computations are conducted with OpenMDAO and MPhys. Stresses and stress derivatives are computed for both the modal displacement method and the modal acceleration method, with the latter shown to be substantially more accurate under prescribed oscillatory loading, for a given number of modes.

Either low-fidelity DLM-based aerodynamics or high-fidelity CFD-based aerodynamics (inviscid) are used to compute the gust loads, deriving oscillatory aerodynamic forces in the frequency domain, and then computing time domain gust response with Fourier transforms. The modal acceleration requires those forces to be in the full-order space, in addition to the typical modal aerodynamics. Differences between modal acceleration and modal displacement are seen for longer gust profiles (but not shorter ones) for a given number of mode shapes. Differences between DLM-based and CFD-based gust stresses are shown to accentuate at higher angles of attack. The increased transonic flow leads to stronger aerodynamic sensitivity for the CFD solver, whereas the unsteady portion of the DLM solver is completely independent of angle of attack.

Strict modal convergence of these gust stresses are not demonstrated here, given challenges with computing unsteady aerodynamics at higher reduced frequencies. For a given number of modes, the computational cost of the modal acceleration formulation is higher than modal displacement: a factor of 3-4 to compute the elastic stresses in the wing, for the cases consid-

ered here, However, modal acceleration will require fewer modes for a given level of accuracy, substantially reducing the computational cost of the CFD-based aeroelasticity.

Finally, the accuracy of the DLM-based adjoint stress derivatives are computed with a finite difference step study, where the companion CFD-based derivatives are left for future work.

5 REFERENCES

[1] Blair, M., "A Compilation of the Mathematics Leading to the Doublet Lattice Method," WL-TR-92-3028, August,1992.

[2] Rodden, W., Johnson, E., "MSC/NASTRAN Aeroelastic Analysis, User's Guide, v68," The MacNeal-Schwendler Corporation, 1994.

[3] Hoblit, F., *Gust Loads on Aircraft: Concepts and Applications*, AIAA, Washington DC, 1988.

[4] Anon., *Part 25: Airworthiness Standards: Transport Category Airplanes*, *CFR14 of the Code of Federal Regulations*, 1964, https://www.faa.gov/documentLibrary/media/Advisory_Circular/AC_25_341-1.pdf

[5] Moreno, R., Narisetti, R., von Knoblauch, F., Taylor, P., "A Modification to the Enhanced Correction Factor Technique to Correlate with Experimental Data," *AIAA SciTech Forum*, Kissimmee, FL, January 2015, https://doi.org/10.2514/6.2015-1421.

[6] Raymer, D., Wilson, J., Perkins, D., Rizzi, A, Zhang, M., Ramirez Puentes, A., "Advanced Technology Subsonic Transport Study: N+3 Technologies and Design Concepts," NASA TM-217130, 2011.

[7] Wales, C., Valente, C., Cook, R., Gaitonde, A., Jones, D., Cooper, J., "The Future of Non-Linear Modeling of Aeroelastic Gust Interaction," *AIAA Aviation Forum*, Atlanta, GA, June 2018, https://doi.org/10.2514/6.2018-3632.

[8] Neumann, J., Mai, H., "Gust Response: Simulation of an Aeroelastic Experiment by a Fluid-Structure Interaction Method," *Journal of Fluids and Structures*, Vol. 38, pp. 290-302, 2013, 10.1016/j.jfluidstructs.2012.12.007.

[9] Huntley, S., Jones, D., Gaitonde, A., "Aeroelastic Gust Response of an Aircraft using a Prescribed Velocity Method in Viscous Flows," *AIAA Aviation Forum*, Denver, CO, June 2017, https://doi.org/10.2514/6.2017-3616.

[10] Guruswamy, G., "Computation of Gust Induced Responses of an Air Taxi by Using Navier-Stokes Equations," *Aerospace Science and Technology*, Vol. 127, 107684, 2022, https://doi.org/10.1016/j.ast.2022.107684.

[11] Jacobson, K., "Adjoint-Based Aeroelastic Optimization with High-Fidelity Time-Accurate Analysis," PhD Thesis, Georgia Institute of Technology, 2018.

[12] Thormann, R., Widhalm, M., "Linear-Frequency-Domain Predictions of Dynamic-Response Data for Viscous Transonic Flows," *AIAA Journal*, Vol. 51, No. 11, pp. 2540-2557, 2013, https://doi.org/10.2514/1.J051896.

[13] Bekemeyer, P., Thormann, R., Timme, S., "Frequency-Domain Gust Response using Computational Fluid Dynamics," *AIAA Journal*, Vol. 55, No. 7, pp. 2154-2187, 2017, https://doi.org/10.2514/1.J055373.

[14] Jacobson, K., Thelen, A., Stanford, B., "Linearized Frequency-Domain Gust Analysis and Adjoint-Based Sensitivities," *AIAA SciTech Forum*, Orlando, FL, January, 2024, https://doi.org/10.2514/6.2024-2591.

[15] Thelen, A., Stanford, B., Jacobson, K., "Flutter and Stochastic Gust Constraint Studies of the Undeflected CRM using MPhys," *AIAA SciTech Forum*, Orlando, FL, January 2024, https://doi.org/10.2514/6.2024-2774.

[16] Kaiser, C., Quero, D., Nitzsche, J., "Quantification of Nonlinear Effects in Gust Load Prediction," *International Forum on Aeroelasticity and Structural Dynamics*, Savannah, GA, June 2019.

[17] Blelloch, P., "Calculation of Structural Dynamic Forces and Stresses using Mode Acceleration," *AIAA Journal*, Vol. 12, No. 5, pp. 760-762, 1988, https://doi.org/10.2514/3.20475.

[18] Livne, E., Blando, G., "Reduced Order Design-Oriented Stress Analysis using Combined Direct and Adjoint Solutions," *AIAA Journal*, Vol. 38, No. 5, pp. 898-909, 2000, https://doi.org/10.2514/2.1045.

[19] de la Fuente, E., "Von Mises Stresses in Random Vibration of Linear Structures," *Computers and Structures*, Vol. 87, No. 21, pp. 1253-1262, 2009, 10.1016/j.compstruc.2009.06.008.

[20] Anderson, W., Biedron, R., Carlson, J., Derlaga, J., Diskin, B., Druyor, C., Gnoffo, P., Hammond, D., Jacobson, K., Jones, W., Kleb, B., Lee-Rausch, E., Liu, Y., Lohry, M., Nastac, G., Nielsen, E., Padway, E., Park, M., Rumsey, C., Thomas, J., Thompson, K., Walden, A., Wang, L., Wood, S., Wood, W., Zhang, X., "FUN3D Manual: 14.2," NASA TM-2025-0002308.

[21] Jacobson, K., Stanford, B., Wood, S., Anderson, W., "Frequency-Domain Flutter Analysis and Sensitivities with Stabilized Finite Elements," *AIAA SciTech Forum*, Orlando, FL, January 6-10, 2020, https://doi.org/10.2514/6.2020-0403.

[22] Engelsen, F., Livne, E., "Modal Acceleration Based Random Gust Stresses in Aeroservoelastic Optimization," *Journal of Aircraft*, Vol. 41, No. 2, pp. 335-347, 2004, https://doi.org/10.2514/1.9329.

[23] Stanford, B., "Aeroservoelastic Optimization under Stochastic Gust Constraints," *Journal of Aeroelasticity and Structural Dynamics*, Vol. 6, No. 1, 2018.

[24] Gray, J., Hwang, J., Martins, J., Moore, K., Naylor, B., "OpenMDAO: An Open-Source Framework for Multidisciplinary Design, Analysis, and Optimization," *Structural and Multidisciplinary Optimization*, Vol. 59, No. 4, pp. 1075-1104, 2019, https://doi.org/10.1007/s00158-019-02211-z.

[25] Yildirim, A., Jacobson, K., Anibal, J., Stanford, B., Gray, J., Mader, C., Martins, J., Kennedy, G., "MPhys: A Modular Multiphysics Simulation Library Using the OpenMDAO Framework," *Structural and Multidisciplinary Optimization*, Vol., 68, No. 1, 2025, https://doi.org/10.1007/s00158-024-03900-0.

[26] Kreisselmeier, G., Steinhauser, R., "Systematic Control Design by Optimizing a Vector Performance Index", *International Federation of Active Controls Symposium on Computer-Aided Design of Control Systems*, Zurich, Switzerland, 1979.

[27] Anderson, W., Newman, J., Karman, S., "Stabilized Finite Elements in FUN3D," *Journal of Aircraft*, Vol. 55, No. 2, pp. 696-714, 2017, https://doi.org/10.2514/1.C034482.

[28] Kiviaho, J., Kennedy, G., "Efficient and Robust Load and Displacement Transfer Scheme using Weighted Least Squares" *AIAA Journal*, Vol. 57, No. 5., pp. 2238-2243, 2019, https://doi.org/10.2514/1.J057318.

[29] Nelson, R., "Simplified Calculation of Eigenvector Derivatives," *AIAA Journal*, Vol. 14, pp. 1201-1205, 1976, https://doi.org/10.2514/3.7211.

[30] Gray, A., Martins, J., "A Proposed Benchmark Model for Practical Aerostructural Optimization of Aircraft Wings" *AIAA SciTech Forum*, Orlando, FL, January 8-12, 2024, https://doi.org/10.2514/6.2024-2775.

[31] Brooks, T., Kenway, G., Martins, J., "Benchmark Aerostructural Models for the Study of Transonic Aircraft Wings," *AIAA Journal*, Vol. 56, No. 7, pp. 2840-2855, 2018, https://doi.org/10.2514/1.J056603.